Journal of Materials Chemistry A

ROYAL SOCIETY OF CHEMISTRY

PAPER

View Article Online
View Journal | View Issue

Cite this: J. Mater. Chem. A, 2020, 8, 25951

A thermally reduced graphene oxide membrane interlayered with an *in situ* synthesized nanospacer for water desalination†

Hongyu Ma,[a] Xiaofang Chen,[a] Shabin Mohammed,[a] Yaoxin Hu,[a] Jun Lu,[a] George P. Simon,[b] Hongjuan Hou[c] and Huanting Wang *[a]

Received 10th June 2020
Accepted 22nd November 2020

DOI: 10.1039/d0ta05790h

rsc.li/materials-a

The interlayer nanostructure of two-dimensional lamellar membranes is important with regard to efficient water permeation and purification. In this work, a new strategy of site-directed incorporation of Prussian blue (PB) nanoparticles into a thermally reduced graphene oxide (rGO) lamellar membrane was developed to enable high water flux for desalination. The membrane was based on the *in situ* synthesized GO/PB composite nanosheets and a subsequent thermal reduction. In this way, nanoparticles were uniformly coordinated to functionalized regions, while supporting the nanoscale water channels. Moreover, the interlayer distances between the pristine graphene areas were enlarged. This structure simultaneously mitigated the water transport resistance from the remaining oxygen-containing groups and increased the water permeation at the particle-free surfaces. As a result, the composite membrane showed 25 times higher flux than the unmodified rGO membrane and a remarkably competitive evaporation-based desalination performance compared with other state-of-the-art membranes. The applicability of this strategy for producing nanostructured lamellar membranes in high-performance desalination is thus demonstrated.

Introduction

In the past few decades, ensembles of two-dimensional (2D) materials have emerged for use in highly efficient separation processes including water purification, gas separation, ion transport and solvent nanofiltration.[1–3] In particular, 2D nanosheets have been widely used as the building blocks to fabricate 2D lamellar membranes possessing cascading, slit-like nanochannels with tunable spacing and controllable physicochemical properties.[4,5] The rational design of 2D lamellar membranes with size sieving effects and molecular interactions allows for the production of membranes with superior selectivity. Furthermore, the stacking of the nanosheets is favourable for scalable ultrathin membrane fabrication, which significantly reduces the permeation resistance and is desirable for high productivity.[5,6]

For water purification, most of the 2D lamellar membranes have the interlayer spacings close to 1 nanometer, which is smaller than the material to be retained, such as dye molecules and salt ions.[1,3,5] Nonetheless, the lamellar membranes with uniform narrow spacings result in long transport paths and slow water permeance due to severe spatial restrictions.[1,5,7] To improve productivity without sacrificing rejection, a common solution is to intercalate nanomaterials as spacers between the nanosheets, which include nanoparticles,[8–14] nanostrands,[15–18] and nanosheets.[19,20] These incorporated nanomaterials are able to enlarge the overall interlayer spacing of the lamellar membranes by forming an architecture of wide channels with curved surrounding nanosheets. Interestingly, some spacers can be removed to create more voids to further enhance the water permeation.[13,15] However, it is hard to retain these voids with the original shape and size after the removal, and the compression due to the applied mechanical pressure can compromise the improvements in flux.[21,22] Alternatively, by retaining these nanomaterials in the lamellar structure, the nanospacers can continuously support the morphology of the constructed channels and prevent the compression of the interlayers.[8–10,14,17–20] Nonetheless, the incorporation of nanomaterials reported so far has mostly relied on physical mixing, which was unfavourable for uniform intercalation.

While most of the 2D lamellar membranes were applied in pressure-driven filtration,[1,5] the rejection of small ion salts was largely unsatisfactory, and they were not very practical in treating high salinity solution due to the high osmotic pressure.[23,24] In contrast, evaporation-based desalination methods,

[a]Department of Chemical Engineering, Monash University, Clayton, Victoria 3800, Australia. E-mail: Huanting.Wang@monash.edu

[b]Department of Materials Science and Engineering, Monash University, Clayton, Victoria 3800, Australia

[c]Energy and Environment Research Institute, Baosteel Group Corporation, Shanghai 201900, China

† Electronic supplementary information (ESI) available. See DOI: 10.1039/d0ta05790h

including membrane distillation (MD) and pervaporation (PV), rely on the vapour pressure difference.[23,24] Therefore, they are promising for treating high concentration saltwater and have the potential to be integrated with renewable energies and zero liquid discharge applications.[24–26] The majority of the MD and PV membranes are polymeric;[23,27,28] however, the low porosity of dense polymer membranes and pore wetting in the MD process impede fast water vapour transport,[28,29] and the large thickness of the selective layer leads to limited PV desalination performance.[23]

Graphene is one of the 2D materials capable of being fabricated into ultrathin membranes with 2D carbon nanochannels for frictionless water transport.[7,30,31] Recently, a multilayer graphene membrane was developed for a direct contact membrane distillation (DCMD) process.[32] The overlapping area of the graphene nanosheets enabled effective water evaporation and permeation, which reached a maximum flux of 50 L m^{-2} h^{-1} (LMH) when treating high saline solution. However, the uniform and narrow spacing of the intrinsic graphene membrane still inhibited the rapid water transport.[7] While graphene nanosheets are challenging to be directly manipulated on a large scale, graphene oxide (GO) nanosheets with pristine graphene domains provide broad possibilities owing to their versatile functional groups and their ease of dispersibility in a number of solvents.[4] Although an unmodified GO membrane is susceptible to swelling in water,[33] the reduced GO membrane can resist the swelling[34] and regain some of the graphene domains.[35] To further improve the water permeation, various nanospacers have been incorporated into reduced GO lamellar membranes.[8,19,20] Nonetheless, most of the nanospacers have been directly mixed with nanosheets for membrane fabrication, which could result in the uneven distribution of the nanomaterials, leaving some parts of the membrane unmodified. Moreover, the neglected functional groups at the narrow 2D channels would impede fast water transport due to the intermolecular interaction.[36–38] Therefore, a uniformly intercalated reduced GO membrane, with enlarged frictionless transport regions and nanospacers supporting wide, internal channels in regions of functionalization, is desirable for high performance desalination.

In this work, we report a new strategy of site-directed incorporation of Prussian Blue (PB) nanoparticles into a thermally reduced graphene oxide (rGO) membrane for high flux evaporation-based desalination. PB crystals are composed of cubic three-dimensional frameworks with alternating coordination between ferrous, ferric and cyanide ions,[39] and possess a porous structure and can be variously synthesized.[40] Therefore, PB was chosen as the spacer of the rGO lamellar membrane. The *in situ* synthesis of PB within the ensemble of the GO nanosheets is directed by the oxygen-containing functional groups. Thus, small PB nanoparticles of uniform size attached on GO nanosheets, with coordination to the regions of functionalization. By a facile vacuum filtration method, a GO/PB composite lamellar membrane can be fabricated. After thermal reduction in argon to remove the majority of hydroxide groups, the membrane becomes hydrophobic, with widened interlayer spacing and nanoparticles supporting the water channels. The transport resistance of water due to the residual functional groups is mitigated owing to the broad channels directly constructed by nanoparticles, and the water flow between the pristine graphene domains is increased with the overall enlarged spacing. As a result, the rGO/PB membranes exhibited high flux up to 202 LMH at 70 °C as the feed temperature, with >99.9% rejection for 3.5 wt% NaCl solution. This represents a facile design of a specially structured lamellar membrane with high performance with regard to membrane desalination.

Results and discussion

In order to directly incorporate the PB particles onto the functionalized regions of GO nanosheets, the *in situ* synthetic method of PB directed by active sites on graphene oxide nanosheets was used.[41,42] Although the PB particles could be directly assembled by the Fe^{2+} and $[Fe(CN)]^{3-}$ ion coordination, this method resulted in uncontrolled growth of large PB particles (Fig. S1a†). This large and uneven size distribution of PB particles is an impediment to the formation of a thin and uniform membrane. In this case, more layers of stacking are required to embed the particles in the selective layer, which could increase the thickness of the membrane and result in low permeation of water. Alternatively, by involving the GO nanosheets in the PB synthesis reaction, the particle size could be well controlled and the formation of large PB particles in solution could be inhibited.

The membrane fabrication is illustrated in Fig. 1a. In the *in situ* reaction, the Fe^{3+} ions were first coordinated with the oxygen-containing functional groups on the GO nanosheets by their spontaneous adsorption of metal ions.[43–45] Then, the GO reduced the Fe^{3+} ions to Fe^{2+}, while coordinating with the dissociative $[Fe(CN)]^{3-}$ and forming small crystals (Fig. S1b†) with a narrow particle size distribution (Fig. S2a†). In this way, small PB particles were directed to form on the functionalized regions of the GO nanosheets. The reaction was allowed to proceed for 6 hours to prevent the over-oxidization of GO and the formation of larger particles. Then, the homemade porous aluminum oxide (Al_2O_3) substrate (Fig. S3†) was applied as the membrane support due to its excellent thermal and mechanical stability. The reaction solution was directly filtered on the substrate, and subsequently rinsed with deionized water to remove the excess ions (Fig. 1a). After fully drying, the GO/PB membrane was reduced in argon at 300 °C for 2 hours, with the thermally reduced membranes being denoted as rGO/PB. Compared with the chemical reduction method of GO, thermal reduction is capable of removing various oxygen-containing groups without the usage of toxic reactants such as hydrazine.[46] The reduction temperature of 300 °C can acceptably remove most of the GO functional groups,[47] while a higher temperature treatment is more energy intensive and would make the membrane fragile.[48] Therefore, a specially structured rGO lamellar membrane with site-directed intercalation of PB nanoparticles was fabricated.

From the top view of the rGO/PB membrane, small nanoparticles were distributed on the surface, as well as in between

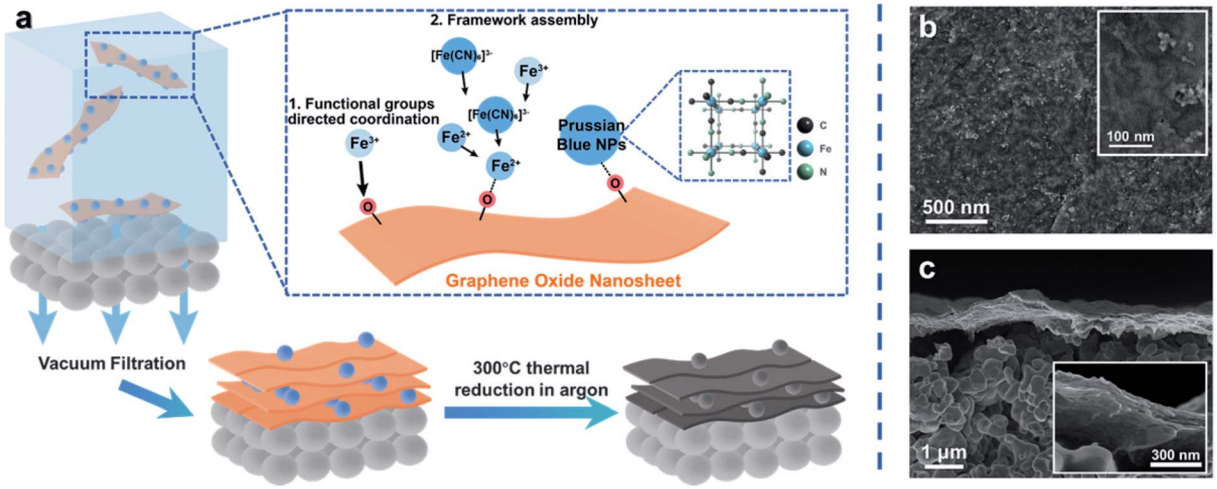

Fig. 1 Membrane fabrication and membrane morphology. (a) Schematic illustration of the fabrication steps of the nanoparticle (NP) intercalated rGO membrane. The *in situ* synthesized GO/PB nanosheets were directly filtered on a porous Al_2O_3 substrate. The thermal reduction in argon was used to remove most of the functional groups in the membrane. (b) Scanning electron microscopy (SEM) image of the top view of the reduced membrane, with the presence of the nanoparticles and the supported channels. (c) SEM image of the cross-sectional view of the membrane, indicating a lamellar structure and a thickness of ~110 nm.

the layers (Fig. 1b). Owing to the flexibility, the rGO nanosheets were distorted in a conformal fashion around the nanoparticles by stacking with each other, creating a tunnel-like structure, which also existed in the interior of the membrane (Fig. S4†). The membrane cross-section shows a typical lamellar structure with a thickness of ~110 nm (Fig. 1c). It can be seen that the moderate intercalation of nanoparticles did not significantly influence the stacking of the nanosheets, and no major defects can be observed. The Fe element was distributed rather evenly in the cross-section of the rGO/PB membrane (Fig. S5†), which proves that the nanoparticles have been attached to rGO nanosheets uniformly and no large crystals were synthesized in the solution during the *in situ* reaction. The concentration of the nanoparticles attached on the nanosheets can be controlled by changing the concentration of the PB reactants during the *in situ* synthesis (Fig. S6†), and a higher concentration of reactant would increase the density of the particles. However, an excessive concentration of reactants resulted in a slight agglomeration of GO/PB composite nanosheets during the reaction and larger PB particles (Fig. S6d†). To retain the uniform structure of the membranes, the optimized membrane was found to be membrane 10 : 8. In addition, the particle size did not have a significant change after the thermal reduction (Fig. S2c and d†), which is favourable for a stable stacking of the nanosheets and a crack-free membrane structure.

For the unmodified GO membrane, the interlayer (d) spacing is around 0.79 nm, according to a relatively sharp peak at 11.2° from the X-ray diffraction (XRD) results (Fig. 2a), which is similar to the previous reports.[33,49,50] After the intercalation of the PB particles, the peak shifts to 10.4° with a notable broadened range (from 6.2° to 14.6°), which indicates the increase in size and a wider size distribution of interlayer spacing. A similar case exists for the reduced membranes. While the main peak of the rGO membrane is at 20.7° (d spacing of 0.43 nm), the peak for the rGO/PB membrane is significantly changed to a range from 14.6° to 26.9°. Compared with the GO membrane, the reduced functional moiety concentration of the rGO reduced the d spacing of the membrane.[51] For rGO/PB membranes, some parts of the functionalized regions of rGO are curved around the PB particles, which creates wide interior channels with a less ordered packing. Thus, the spacings of these space-induced channels in the lamellar membrane are not observable in XRD results which required a layered order.[8,13,14] To further characterize the membrane pores, the rGO/PB membrane was characterized with argon adsorption and the pore size distribution was calculated (Fig. S9†). The wide channels of around 10 nm were directly constructed by the nanoparticles, followed by the transition area with sizes ranging from about 3 nm to 10 nm. Furthermore, the intercalation of the nanoparticles also considerably widened the interlayer spacings of the particle-free area to around 1.7 nm (illustrated in Fig. 2d). The incorporation of the PB nanoparticles in the GO/PB membrane was confirmed by the XRD (200) characteristic peak at ~17.8° (Fig. 2a and S7†). To further investigate the particles' crystallinity change during the thermal treatment, membrane samples with an excess amount of PB particles (GO/mPB and rGO/mPB) were characterized by XRD (Fig. S7†). The variation of the XRD peaks indicated that PB particles were decomposed and possibly oxidized by the GO,[47] and it mainly resulted in Fe_3O_4 nanoparticles in the lamellar structures, which was also in accordance with the X-ray photoelectron spectroscopy (XPS) results (Fig. S8†). Therefore, the role of the nanoparticles within the reduced membrane was mainly a structural support for the wide channels and enlarged spacings.

The Fourier-transform infrared spectroscopy (FT-IR) pattern of the GO shows that the oxygen-containing functional groups on GO are mainly hydroxyl, carbonyl, carboxylic, and epoxide (Fig. 2b).[52] After the PB synthesis, sharp absorption peaks at

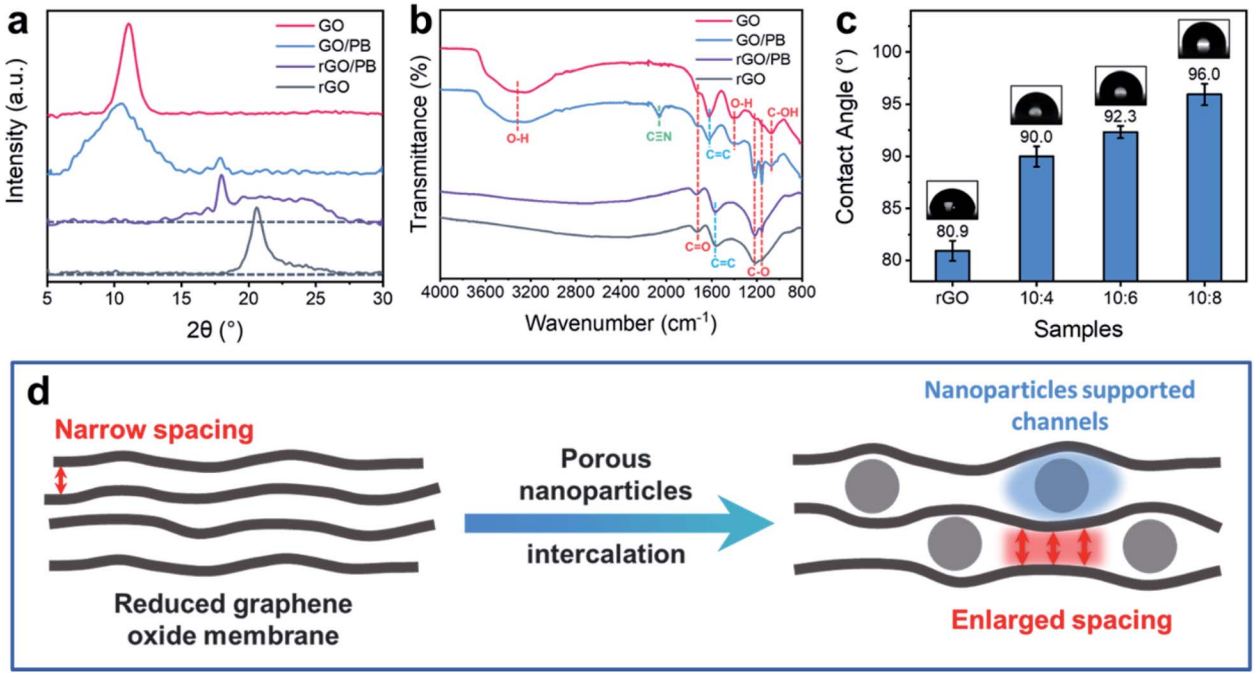

Fig. 2 Characterization of the GO/PB membrane before and after thermal reduction. (a) XRD results of membranes with different compositions. The GO/PB and rGO/PB membranes were fabricated under the same reaction conditions as membrane 10 : 8. The shifted and broadened peaks indicated the enlargement of the interlayer spacing. (b) FT-IR patterns of the membranes, confirming the reductant role of GO and the removal of most of the functional groups during thermal reduction. (c) The contact angle measurements of the membranes after thermal reduction with increasing addition of PB particles. (d) Schematic illustration of the role of intercalated PB nanoparticles.

1153 and 1226 cm^{-1} show the increased intensity of C–O stretching, which confirms the GO's role of being a reductant during the reaction, while possibly generating extra epoxide and hydroxyl groups. Another additional absorption peak of GO/PB is at 2064 cm^{-1}, which could be attributed to the stretching of cyanide groups (CN) from PB particles.[53] After the thermal reduction, the CN characteristic peak of PB disappeared, indicating the decomposition of the PB particles. For the rGO membrane, the absorption peaks of hydroxyl groups are eliminated, which results in the slight hydrophobicity with a water contact angle (WCA) of ~80.9° (Fig. 2c and S10†). When comparing the rGO membrane with rGO/PB membranes, there was an increasing trend of the contact angle with more intercalation of the nanoparticles, which increased up to 96.0°. Considering that the rGO/PB membranes had slightly more C–O bonds than the rGO membrane (Fig. 2b), the increase in the contact angles was most possibly due to the production of nanoscale surface patterns upon the incorporation of the nanoparticles (Fig. S6†).[54,55] Similar strategies of applying surface roughness for improvement of hydrophobicity have been previously demonstrated in graphene-based materials[56,57] and various membrane studies.[58–60]

To evaluate the effects of the nanoparticle-supported channels and the enlarged spacing, the membranes were sealed with Kapton tape and epoxy glue and mounted on a vacuum filtration setup (Fig. S11†) to carry out the vacuum assisted evaporation-based process. According to all the test results, the conductivity of the condensed, permeated water was below 1.8 μS cm^{-1} at room temperature (~20 °C), which represented a salt rejection of >99.9%. This was in accordance with the ideal 100% salt rejection based on water evaporation.[28] With some wrinkled structures (Fig. S12†), the unmodified rGO membrane showed a flux of 0.6 LMH when treating 3.5 wt% NaCl solution at room temperature (Fig. 3b). This limited performance is mainly due

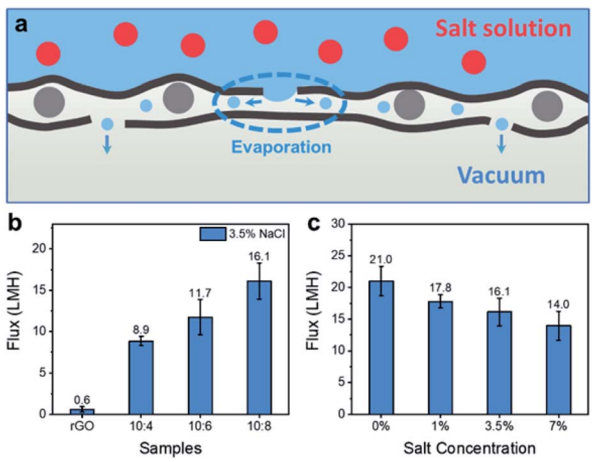

Fig. 3 Desalination performance at room temperature. (a) Schematic illustration of the proposed separation and transport mechanism of the desalination process. Red dots represent the salt in solution, and light blue dots represent the water vapor. (b) Flux results for 3.5 wt% NaCl solution of membranes with increasing addition of PB particles at room temperature (~20 °C). (c) Flux results of membrane 10 : 8 for NaCl solution with different concentrations at room temperature.

to the close spacing between the rGO nanosheets,[7] while the remaining oxygen-containing functional groups could also resist the rapid water transport due to the hydrogen bonding.[37] After the incorporation of the nanoparticles, the flux increased up to 16.1 LMH, which was 25 times that of the unmodified rGO membrane without sacrificing the rejection. The higher additions of PB particles could induce higher fluxes (Fig. 3b). The possible reason is that the incorporation of more particles could support more channels, which made them more likely to be interconnected and water transportation through the narrower regions could thus be reduced.

The proposed separation mechanism is illustrated in Fig. 3a. When the feed solution is in contact with the membrane, the nanoscale carbonaceous entrance impedes the direct penetration of liquid water with its slight hydrophobicity (Scheme S1†).[61] Therefore, water evaporation occurs and the water permeates in the form of vapour, which is a membrane distillation process. With the assistance of a vacuum, the water vapour is rapidly transported through the structured membrane. The potential negative impact from the remaining functional groups is mainly mitigated by the nanoparticle-supported channels, which have widths of several nanometers. The water permeation through the pristine graphene regions is further increased with the enlarged spacing. The rGO/PB is also capable of treating a high concentration salt solution of 7 wt% (Fig. 3c), which is the typical salinity of RO brine.[62] However, compared with pure water flux, there was a noticeable flux decline for the treatment of 7 wt% NaCl solution. This is likely due to the concentration polarization. As the water evaporates, the solution near the narrow entrance of the membrane is considerably concentrated. While the vacuum is extracting the rest of the solution, the excess salt is unable to be fully diffused due to the water flow. This results in decreased water concentration near the entrance, which decreases the overall flux. The performance also depends significantly on the thickness of the membrane (Fig. S13†). Reduced thickness represents less transport distance throughout the membrane, and thus higher flux. Conversely, despite the incorporation of the nanoparticles, a continuous and defect-free lamellar membrane still requires several layers of nanosheets to be properly stacked with each other. Therefore, the optimal membrane thickness was found to be ~110 nm.

The rGO/PB membrane was further evaluated by measuring the pure water and salt solution fluxes under heating conditions (Fig. 4a). The feed solution was heated with a heating plate and circulated onto the membrane with a peristaltic pump (Fig. S11†). The temperature of the feed solution was measured using a thermometer and controlled accordingly by adjusting the heating plate, which had a fluctuation of less than 3 °C. The increasing temperature could significantly increase the vapour pressure of water, which boosts the evaporation process and considerably enhances the water flux. Consequently, at 70 °C, the pure water flux reached 264.6 LMH, and the flux for desalination of the 3.5 wt% NaCl solution was 202.2 LMH. The major flux difference between pure water and salt water indicates that the concentration polarization became more severe with increased levels of flux.[61] Nonetheless, the desalination performance of the rGO/PB

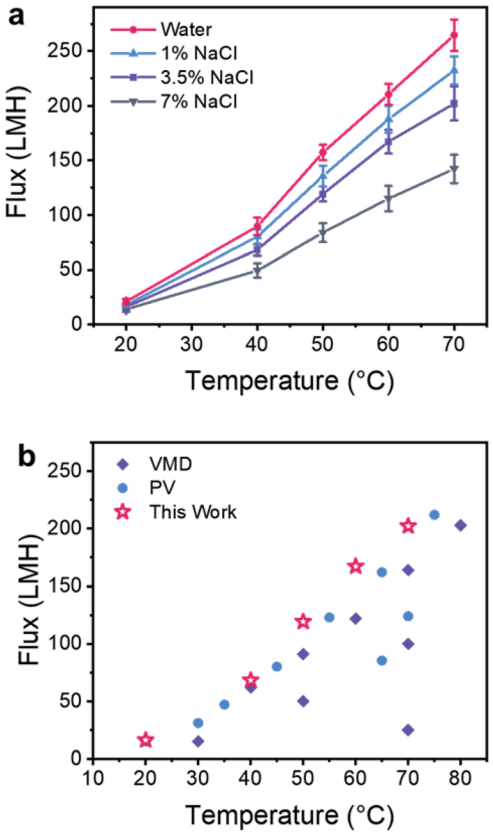

Fig. 4 Desalination performance under heating conditions. (a) The desalination fluxes of NaCl solution with different concentrations from 20 °C to 70 °C tested with membrane 10 : 8. (b) The comparison of the 3.5 wt% NaCl desalination performance in this work with the literature (Table S1†).

membrane is remarkably competitive with other state-of-the-art membrane processes based on vacuum-assisted water evaporation including vacuum membrane distillation (VMD)[61,63,64] and PV[65–67] (Fig. 4b and Table S1†). Moreover, compared with other nanomaterial-intercalated rGO membranes (Table S2†),[17,57,68–73] the rGO/PB membrane is very advantageous in salt rejection when treating high salinity solution at room temperature, while the heating conditions could further boost the flux and the desalination efficiency. The fluxes of the present work are either close or higher than the performance of other state-of-the-art membranes, which demonstrated the high water transport capacity of this specially structured rGO membrane and its applicability in high-performance desalination. Note that our current membrane is not suitable for operation in direct contact membrane distillation mode (Fig. S14†), so more work is needed to further address this limitation by possibly applying versatile nanomaterials or introducing post-synthesis modifications.

Experimental section

Materials

Alumina powder (Hangzhou Jikang New Material) and polyvinyl alcohol (PVA, Sigma-Aldrich) were used for substrate

fabrication. Ferric chloride ($FeCl_3$, Sigma-Aldrich) and potassium ferricyanide ($K_3[Fe(CN)_6]$, Sigma-Aldrich) were the reactants for the *in situ* synthesis of Prussian blue. The pH of the reaction solution was regulated with hydrochloric acid (HCl, 32% solution, Merck). The salt solutions for performance evaluation were prepared with sodium chloride (NaCl, Merck). All chemicals were used as received, without further purification.

Preparation of the Al_2O_3 substrate

Ceramic substrates were prepared by tabletting an Al_2O_3 powder and polyvinyl alcohol (PVA) mixture and sintering at high temperature. In detail, 10 g of α-Al_2O_3 powder was first ground with dropwise addition of ~1.5 ml of 10 wt% PVA water solution for around 2 hours. After sufficiently mixing and milling, 2.7 g of the powdery mixture was tableted at 10 MPa pressure for 1 minute, resulting in a hardened disc with 30 mm diameter and ~2 mm thickness. The sintering of the substrates was carried out in air according to the following steps: the temperature was first raised to 800 °C at 1 °C min^{-1} and maintained for 1 hour, and then it was further increased to 1350 °C and held for 2 hours for fully sintering. After cooling down to room temperature, the substrates were rinsed with running water and then polished with sandpaper (P1200, WS Flex 16, Hermes) to achieve a relatively flat surface.

In situ synthesis of Prussian blue nanoparticles on graphene oxide nanosheets

A GO aqueous dispersion was first prepared with a modified Hummers method.[74] A typical *in situ* reaction solution included 0.001 wt% GO, 0.08 mM $FeCl_3$, and 0.08 mM $K_3[Fe(CN)_6]$ with a pH ≈ 2 (adjusted with HCl solution) environment,[41,42] and the final derived membrane fabricated with the above-mentioned ratio was briefly denoted as 10 : 8. Different concentrations of $FeCl_3$ and $K_3[Fe(CN)_6]$ were also investigated, and membranes fabricated from 0.04 mM and 0.06 mM reactants were denoted as 10 : 4 and 10 : 6, respectively. Then the reaction was carried out by vigorously stirring the solution for 6 h at room temperature. For flux comparison, the unmodified rGO membrane was fabricated with the same loading of GO.

To further characterize the particle components, GO nanosheets were grown with an excess amount of PB particles (denoted as GO/mPB) under the same conditions of 10 : 8 with 24 hour reaction time.

Membrane fabrication and thermal reduction

After the *in situ* synthesis of the GO/PB nanosheets, 4.5 ml of the solution was directly filtered onto the Al_2O_3 substrate with a membrane diameter of 13 mm under a vacuum of ~0.1 bar. The thickness of the membranes could be controlled by applying different volumes of the reactant solution. Then the membrane was carefully rinsed by further filtering ~5 ml of deionized water to remove the excess unbonded reactants. The vacuum was continuously applied overnight to dry the membrane at room temperature. Finally, the membrane was thermally reduced at 300 °C for 2 hours with running argon flow in a tube furnace and a heating rate of 1 °C min^{-1}.

Characterization

SEM images were taken by using a Magellan 400 FEG (FEI, USA), and all samples were coated with iridium prior to the SEM sessions. The SEM operation voltage ranged from 3 kV to 5 kV depending on the charging effects of the samples. TEM images were taken with a Tecnai G2 T20 TWIN LaB6 (FEI, USA) with an operating voltage of 200 kV. TEM samples were prepared by redispersing the filtered membrane in ethanol with ultrasonication, and dropping the dispersion onto a copper grid covered with a carbon film. Wettability of the membranes with different particle loading concentrations was analyzed with a video-based contact angle measuring instrument (Dataphysics OCA15, German). Each sample was tested at at least 5 different locations on the surface, and the results were shown as the average contact angle value. The FT-IR spectra of the membranes were acquired by using an FT-IR Spectrometer (Perkin Elmer Spectrum Two, USA). XRD patterns were recorded using a D2 Phaser (Bruker, USA) with a Cu Kα radiation source (30 kV, 10 mA) and a scanning speed of 2° min^{-1}. XPS characterization was carried out with a Nexsa Surface Analysis System (Thermo Fisher Scientific, USA). An argon adsorption test of the membranes was performed on a 3Flex (Micromeritics, USA) at a temperature of 77 K. And the pore size distribution was calculated based on the density functional theory (slit pore model). For FT-IR, XRD, XPS and argon adsorption analysis, free-standing membrane samples were prepared by filtering ~30 ml reaction solution (same reaction conditions as 10 : 8) and drying under a vacuum. The thermal reduction was carried out by placing the free-standing membrane between two Al_2O_3 substrates.

Desalination performance tests

Before carrying out the tests, the membrane was sealed with Kapton polyimide tape, with the edges covered by resin glue (Torr Seal, Agilent). The experiments were performed using a vacuum filtration setup with a liquid nitrogen trap for condensing water vapour between the permeate side and the vacuum pump. The heated solution with controlled temperature on the feed side was circulated with a peristaltic pump (Fig. S11†). The pressure difference between the two sides of the membrane was ~0.9 bar, indicated by a pressure meter on the vacuum pump. After a certain amount of time, the condensed water was poured out, weighed, and measured with a conductivity meter. The flux could be calculated as:

$$J = \frac{m}{\rho \times t \times A} \quad (1)$$

where J is the overall flux, m is the mass of the condensed water, ρ is the density of water, t is the time of testing duration and A is the effective area of the membrane. For each condition, at least 3 individual membranes were tested.

Conclusions

Functionalized sites on graphene oxide nanosheets were used for *in situ* synthesis and intercalation of PB nanoparticles. Thus,

a thermally reduced, hydrophobic lamellar membrane was successfully produced which could be used in a high flux, evaporation-based desalination process. The uniform, site-directed intercalation of the nanoparticles counteracted the greater water transport resistance arising due to the remaining functional groups by inducing wider channels from the curved rGO nanosheets. Moreover, the enlarged interlayer spacing of the pristine graphene regions enabled the rapid water permeation. Therefore, the rGO/PB achieved an excellent flux of 202 LMH at 70 °C with >99.9% rejection for 3.5 wt% NaCl solution. This simple method allows the possibility of utilising such structured lamellar membranes for rapid hypersaline desalination.

Conflicts of interest

There are no conflicts to declare.

Acknowledgements

This research forms part of the Baosteel Australia Research and Development Centre (BAJC) portfolio of projects and has received support through the Centre (Project no. BA17005) and the Australian Research Council (Project no. IH170100009). Hongyu Ma acknowledges Monash University for the scholarships. The authors acknowledge the technical support for SEM and TEM from the Monash Centre for Electron Microscopy, XRD and XPS from the Monash X-ray Platform, and FTIR and Gas Adsorption from Dr Anthony De Girolamo of the Department of Chemical Engineering, Monash University.

Notes and references

1 S. Wang, L. Yang, G. He, B. Shi, Y. Li, H. Wu, R. Zhang, S. Nunes and Z. Jiang, *Chem. Soc. Rev.*, 2020, **49**, 1071–1089.
2 G. Liu, W. Jin and N. Xu, *Angew. Chem., Int. Ed.*, 2016, **55**, 13384–13397.
3 S. Kim, H. Wang and Y. M. Lee, *Angew. Chem., Int. Ed.*, 2019, **58**, 17512–17527.
4 B. Mi, *Science*, 2014, **343**, 740–742.
5 Y. Kang, Y. Xia, H. Wang and X. Zhang, *Adv. Funct. Mater.*, 2019, **29**, 1902014.
6 G. Liu, W. Jin and N. Xu, *Chem. Soc. Rev.*, 2015, **44**, 5016–5030.
7 R. R. Nair, H. A. Wu, P. N. Jayaram, I. V. Grigorieva and A. K. Geim, *Science*, 2012, **335**, 442–444.
8 K. Guan, D. Zhao, M. Zhang, J. Shen, G. Zhou, G. Liu and W. Jin, *J. Membr. Sci.*, 2017, **542**, 41–51.
9 L. Chen, N. Li, Z. Wen, L. Zhang, Q. Chen, L. Chen, P. Si, J. Feng, Y. Li, J. Lou and L. Ci, *Chem. Eng. J.*, 2018, **347**, 12–18.
10 G. Zhao, R. Hu, X. Zhao, Y. He and H. Zhu, *J. Membr. Sci.*, 2019, **585**, 29–37.
11 M. Zhang, K. Guan, J. Shen, G. Liu, Y. Fan and W. Jin, *AIChE J.*, 2017, **63**, 5054–5063.
12 S. Wang, D. Mahalingam, B. Sutisna and S. P. Nunes, *J. Mater. Chem. A*, 2019, **7**, 11673–11682.
13 L. Ding, Y. Wei, Y. Wang, H. Chen, J. Caro and H. Wang, *Angew. Chem., Int. Ed.*, 2017, **56**, 1825–1829.
14 R. P. Pandey, K. Rasool, V. E. Madhavan, B. Aïssa, Y. Gogotsi and K. A. Mahmoud, *J. Mater. Chem. A*, 2018, **6**, 3522–3533.
15 H. Huang, Z. Song, N. Wei, L. Shi, Y. Mao, Y. Ying, L. Sun, Z. Xu and X. Peng, *Nat. Commun.*, 2013, **4**, 2979.
16 X. Chen, M. Qiu, H. Ding, K. Fu and Y. Fan, *Nanoscale*, 2016, **8**, 5696–5705.
17 Y. Han, Y. Jiang and C. Gao, *ACS Appl. Mater. Interfaces*, 2015, **7**, 8147–8155.
18 Y. Wei, Y. Zhu and Y. Jiang, *Chem. Eng. J.*, 2019, **356**, 915–925.
19 X. Sui, Z. Yuan, C. Liu, L. Wei, M. Xu, F. Liu, A. Montoya, K. Goh and Y. Chen, *J. Mater. Chem. A*, 2020, **3**, 10031–10037.
20 L. Liu, Y. Zhou, J. Xue and H. Wang, *AIChE J.*, 2019, **65**, e16699.
21 Y. Wei, Y. Zhang, X. Gao, Y. Yuan, B. Su and C. Gao, *Carbon*, 2016, **108**, 568–575.
22 H. Huang, Y. Mao, Y. Ying, Y. Liu, L. Sun and X. Peng, *Chem. Commun.*, 2013, **49**, 5963–5965.
23 Q. Wang, N. Li, B. Bolto, M. Hoang and Z. Xie, *Desalination*, 2016, **387**, 46–60.
24 A. Deshmukh, C. Boo, V. Karanikola, S. Lin, A. P. Straub, T. Tong, D. M. Warsinger and M. Elimelech, *Energy Environ. Sci.*, 2018, **11**, 1177–1196.
25 N. Dow, S. Gray, J. de Li, J. Zhang, E. Ostarcevic, A. Liubinas, P. Atherton, G. Roeszler, A. Gibbs and M. Duke, *Desalination*, 2016, **391**, 30–42.
26 W. Wang, Y. Shi, C. Zhang, S. Hong, L. Shi, J. Chang, R. Li, Y. Jin, C. Ong, S. Zhuo and P. Wang, *Nat. Commun.*, 2019, **10**, 3012.
27 L. Eykens, K. De Sitter, C. Dotremont, L. Pinoy and B. Van der Bruggen, *Sep. Purif. Technol.*, 2017, **182**, 36–51.
28 P. Wang and T. S. Chung, *J. Membr. Sci.*, 2015, **474**, 39–56.
29 M. Rezaei, D. M. Warsinger, J. H. Lienhard V, M. C. Duke, T. Matsuura and W. M. Samhaber, *Water Res.*, 2018, **139**, 329–352.
30 B. Radha, A. Esfandiar, F. C. Wang, A. P. Rooney, K. Gopinadhan, A. Keerthi, A. Mishchenko, A. Janardanan, P. Blake, L. Fumagalli, M. Lozada-Hidalgo, S. Garaj, S. J. Haigh, I. V. Grigorieva, H. A. Wu and A. K. Geim, *Nature*, 2016, **538**, 222–225.
31 P. Sun, K. Wang and H. Zhu, *Adv. Mater.*, 2016, **28**, 2287–2310.
32 D. H. Seo, S. Pineda, Y. C. Woo, M. Xie, A. T. Murdock, E. Y. M. Ang, Y. Jiao, M. J. Park, S. Il Lim, M. Lawn, F. F. Borghi, Z. J. Han, S. Gray, G. Millar, A. Du, H. K. Shon, T. Y. Ng and K. Ostrikov, *Nat. Commun.*, 2018, **9**, 683.
33 S. Zheng, Q. Tu, J. J. Urban, S. Li and B. Mi, *ACS Nano*, 2017, **11**, 6440–6450.
34 H. Liu, H. Wang and X. Zhang, *Adv. Mater.*, 2015, **27**, 249–254.
35 G. Eda and M. Chhowalla, *Adv. Mater.*, 2010, **22**, 2392–2415.
36 Y. Han, Z. Xu and C. Gao, *Adv. Funct. Mater.*, 2013, **23**, 3693–3700.

37 J. Deng, Y. You, H. Bustamante, V. Sahajwalla and R. K. Joshi, *Chem. Sci.*, 2017, **8**, 1701–1704.
38 N. Wei, X. Peng and Z. Xu, *ACS Appl. Mater. Interfaces*, 2014, **6**, 5877–5883.
39 B. Kong, J. Tang, Z. Wu, J. Wei, H. Wu, Y. Wang, G. Zheng and D. Zhao, *Angew. Chem., Int. Ed.*, 2014, **53**, 2888–2892.
40 B. Kong, C. Selomulya, G. Zheng and D. Zhao, *Chem. Soc. Rev.*, 2015, **44**, 7997–8018.
41 B. Kong, X. Sun, C. Selomulya, J. Tang, G. Zheng, Y. Wang and D. Zhao, *Chem. Sci.*, 2015, **6**, 4029–4034.
42 E. Jin, X. Lu, L. Cui, D. Chao and C. Wang, *Electrochim. Acta*, 2010, **55**, 7230–7234.
43 R. R. Amirov, J. Shayimova, Z. Nasirova and A. M. Dimiev, *Carbon*, 2017, **116**, 356–365.
44 Y. Lei, F. Chen, Y. Luo and L. Zhang, *Chem. Phys. Lett.*, 2014, **593**, 122–127.
45 X. Yang, X. Zhang, Y. Ma, Y. Huang, Y. Wang and Y. Chen, *J. Mater. Chem.*, 2009, **19**, 2710–2714.
46 X. Gao, J. Jang and S. Nagase, *J. Phys. Chem. C*, 2010, **114**, 832–842.
47 R. Larciprete, S. Fabris, T. Sun, P. Lacovig, A. Baraldi and S. Lizzit, *J. Am. Chem. Soc.*, 2011, **133**, 17315–17321.
48 C. M. Chen, J. Q. Huang, Q. Zhang, W. Z. Gong, Q. H. Yang, M. Z. Wang and Y. G. Yang, *Carbon*, 2012, **50**, 659–667.
49 J. Abraham, K. S. Vasu, C. D. Williams, K. Gopinadhan, Y. Su, C. T. Cherian, J. Dix, E. Prestat, S. J. Haigh, I. V. Grigorieva, P. Carbone, A. K. Geim and R. R. Nair, *Nat. Nanotechnol.*, 2017, **12**, 546–550.
50 F. Zhao, H. Cheng, Z. Zhang, L. Jiang and L. Qu, *Adv. Mater.*, 2015, **27**, 4351–4357.
51 S. H. Huh, in *Physics and Applications of Graphene*, ed. S. Mikhailov, IntechOpen, 2011, pp. 73–90.
52 D. R. Dreyer, S. Park, C. W. Bielawski and R. S. Ruoff, *Chem. Soc. Rev.*, 2010, **39**, 228–240.
53 X. Q. Zhang, S. W. Gong, Y. Zhang, T. Yang, C. Y. Wang and N. Gu, *J. Mater. Chem.*, 2010, **20**, 5110–5116.
54 Y. Tian and L. Jiang, *Nat. Mater.*, 2013, **12**, 291–292.
55 X. Feng and L. Jiang, *Adv. Mater.*, 2006, **18**, 3063–3078.
56 J. N. Wang, R. Q. Shao, Y. L. Zhang, L. Guo, H. B. Jiang, D. X. Lu and H. B. Sun, *Chem.–An Asian J.*, 2012, **7**, 301–304.
57 Y. Mao, Q. Huang, B. Meng, K. Zhou, G. Liu, A. Gugliuzza, E. Drioli and W. Jin, *J. Membr. Sci.*, 2020, **611**, 118364.
58 Y. Liao, R. Wang and A. G. Fane, *J. Membr. Sci.*, 2013, **440**, 77–87.
59 D. Hou, J. Wang, X. Sun, Z. Ji and Z. Luan, *J. Membr. Sci.*, 2012, **405–406**, 185–200.
60 J. E. Efome, M. Baghbanzadeh, D. Rana, T. Matsuura and C. Q. Lan, *Desalination*, 2015, **373**, 47–57.
61 W. Chen, S. Chen, T. Liang, Q. Zhang, Z. Fan, H. Yin, K. W. Huang, X. Zhang, Z. Lai and P. Sheng, *Nat. Nanotechnol.*, 2018, **13**, 345–350.
62 J. M. Arnal, M. Sancho, I. Iborra, J. M. Gozálvez, A. Santafé and J. Lora, *Desalination*, 2005, **182**, 435–439.
63 M. Pagliero, A. Bottino, A. Comite and C. Costa, *J. Membr. Sci.*, 2020, **596**, 117575.
64 K. J. Lu, J. Zuo, J. Chang, H. N. Kuan and T. S. Chung, *Environ. Sci. Technol.*, 2018, **52**, 4472–4480.
65 Y. L. Xue, J. Huang, C. H. Lau, B. Cao and P. Li, *Nat. Commun.*, 2020, **11**, 1461.
66 Y. Song, R. Li, F. Pan, Z. He, H. Yang, Y. Li, L. Yang, M. Wang, H. Wang and Z. Jiang, *J. Mater. Chem. A*, 2019, **7**, 18642–18652.
67 G. Liu, J. Shen, Q. Liu, G. Liu, J. Xiong, J. Yang and W. Jin, *J. Membr. Sci.*, 2018, **548**, 548–558.
68 L. Zhu, H. Wang, J. Bai, J. Liu and Y. Zhang, *Desalination*, 2017, **420**, 145–157.
69 J. Zhu, J. Wang, A. A. Uliana, M. Tian, Y. Zhang, Y. Zhang, A. Volodin, K. Simoens, S. Yuan, J. Li, J. Lin, K. Bernaerts and B. Van Der Bruggen, *ACS Appl. Mater. Interfaces*, 2017, **9**, 28990–29001.
70 R. Han and P. Wu, *J. Mater. Chem. A*, 2019, **7**, 6475–6481.
71 P. Zhang, J. L. Gong, G. M. Zeng, B. Song, H. Y. Liu, S. Y. Huan and J. Li, *Chemosphere*, 2018, **204**, 378–389.
72 E. Yang, A. B. Alayande, C. M. Kim, J. ho Song and I. S. Kim, *Desalination*, 2018, **426**, 21–31.
73 Y. Liu, Z. Yu, Y. Peng, L. Shao, X. Li and H. Zeng, *Chem. Phys. Lett.*, 2020, **749**, 137424.
74 Y. Hu, J. Wei, Y. Liang, H. Zhang, X. Zhang, W. Shen and H. Wang, *Angew. Chem., Int. Ed.*, 2016, **55**, 2048–2052.

